11th International Workshop on Ship and Marine Hydrodynamics
Hamburg, Germany, September 22-25, 2019

CFD Simulations and Model Experiments of Offshore Support Vessel with Heavy Suspended Load in Waves

Motoki Araki[1]*, Kazuhisa Otsubo[1], Kei Ishida[1], Kenta Hasegawa[1], Hiroshi Sato[1], Kunihide Ohashi[2]

[1]National Maritime Research Institute, Ocean Engineering Department
6-38-1 Shinkawa, Mitaka, 181-0004 Tokyo, Japan
[2]National Maritime Research Institute, Fluid Engineering & Ship Performance Evaluation Department
6-38-1 Shinkawa, Mitaka, 181-0004 Tokyo, Japan

*Corresponding author, araki@nmri.go.jp

ABSTRACT

Nowadays, since, subsea equipment becoming larger and heavier, risks of the lifting/lowering operations by offshore support vessel (OSV) are also increasing and thereby predicting coupling motions of the vessel and whirling equipment and hydrodynamic forces acting on the suspended load in splash zone are important to prevent clash accidents and damage on lifted subsea equipment etc. Model experiment using OSV with heavy suspended load was conducted in Deepsea Basin in National Maritime Research Institute (NMRI). The experiments were carried out with several regular and irregular waves and heading angles. The OSV was moored with 4 lined spring system. During the experiments, the motions of moored OSV and suspended load were measured with visual 3D motion capture system. Computation fluid dynamics (CFD) simulations were conducted using CFD Solver NAGISA which was developed in NMRI to investigate the dynamics and hydrodynamical aspects. Dynamic overset grid method and multibody dynamics model were applied to reproduce the coupling motions of the vessel and suspended load. The CFD simulations were carried out when the suspended load is in the splash zone to predict hydrodynamic forces acting on the lifted equipment. The CFD simulation results were validated with the model experiment comparing with motions of OSV and suspended load.

1 INTRODUCTION

In these days, subsea production system becomes more and more complicated and enlarges its size which increases the scale and complexity of offshore constructions. During the offshore construction, OSV has essential roles especially on lifting/lowering operation such as installing and removal of subsea equipment. However, the lifting/lowering operation with heavy suspended load in offshore condition could be dangerous for human and equipment since whirling motion of suspended load coupled with vessel motion seems to be unpredictable in harsh weather. Waiting for calm weather for safe lifting/lowering operation could tight up the construction schedule. Therefore, predicting dynamic behaviour of suspended load could improve the safety and availability of the OSV lifting/lowering operation.

In 1980's, Schellin et al. [1] had linearized analysis in the frequency domain coupling motions of shear-leg crane vessel and heavy payload in head waves. Recently, dynamic simulation in time domain becomes dominant in this research topic since linearized model is not enough to treat non-linear coupling motions of vessel and suspended load. Hannan and Bai [2] simulated the motion of cylindrical payload suspended by crane barge with boundary element method to clear the shielding effect of vessel during the lifting/lowering operation while only pendulum motion of the suspended load was considered and had no coupling motion with crane barge. Hong et al [3] built elastic crane model based on finite element method and multibody dynamics for coupling with OSV motion in time domain while hydrodynamic forces were pre-calculated with WADAM

by DNV in frequency domain. Many other studies have been done applying potential theory for hydrodynamic computation, e.g. [4], [5]. However, most of subsea equipment are usually non-streamlined shape, which could generate large vortex shedding from the edges which is important to predict hydrodynamic force which indicates that potential theory could be not accurate enough to obtain hydrodynamic force on suspended load. Solaas et al [6] computed hydrodynamic force on payload using viscous CFD during lowering operation to obtain viscous damping and added mass which had no dynamic coupling with ship motions. Therefore, in this research, multibody dynamics (MBD) solver is developed and integrated into CFD solver to simulate dynamic coupling of CFD and MBD to develop simulation tool for marine operations.

2 MODEL EXPERIMENT

The motion characteristics in wave for the OSV with suspended load was investigated in Deepsea Basin of NMRI. The purpose of this model experiment is to understand the fundamental phenomenon for the coupled motion between OSV and suspended load and provides the validation data for CFD simulation.

2.1 Models

In this paper the standard OSV model for multi-purpose is investigated experimentally because it is popular vessel in offshore construction field. The size of OSV is determined as Table 1 since similar OSV size are dominant in the world [7]. This OSV has large crane on starboard side stern deck. The suspended load is assumed to be rectangular shape to simplify the hydrodynamical problem. These principal dimension and appearance are shown in Table 1 and Figure 1 respectively. These models are 1/30 scaled.

Table 1: Principal dimensions for OSV and suspended load (1/30 Scaled).

Items	Items	Full Scaled	Model Scaled	Note
OSV	Length overall: L_{OA}	78.00 m	2.60 m	Operational Condition
	Length between perpendiculars: L_{PP}	75.20 m	2.51 m	
	Breadth: B	21.50 m	0.72 m	
	Depth: D	7.50 m	0.23 m	
	Draft: d	5.61 m	0.19 m	
	Displacement: Δ	6623 ton	239 kg	
Suspended Load	Length: L_{SP}	12.0 m	0.40 m	
	Breadth: B_{SP}	3.6 m	0.12 m	
	Depth: D_{SP}	4.5 m	0.15 m	
	Mass in air: M_{SP}	261 ton	9.70kg	

Figure 1: Pictures of OSV (left and center) and suspended load models (right).

2.2 Experimental Setup and Conditions

The OSV model was moored by 4 mooring (wire + spring) lines to prevent from drifting in wave and to be located around the centre of the basin. Figure 2 is shown to depict the configuration of mooring system and experimental setup in the basin. To measure the 3D-motion by camera system, three coloured markers were attached on the both the OSV and the suspended load. The 3D-location data for these markers were analysed to transform to each centre of gravity (CoG). Table 2 shows the experimental wave condition. Added to this experiment, free oscillation tests were also conducted to investigate the damping ratio and the natural frequency for OSV model. Here definition of wave angle 0 deg. is following wave, 90 deg. is beam wave from starboard side, 180 deg. head wave.

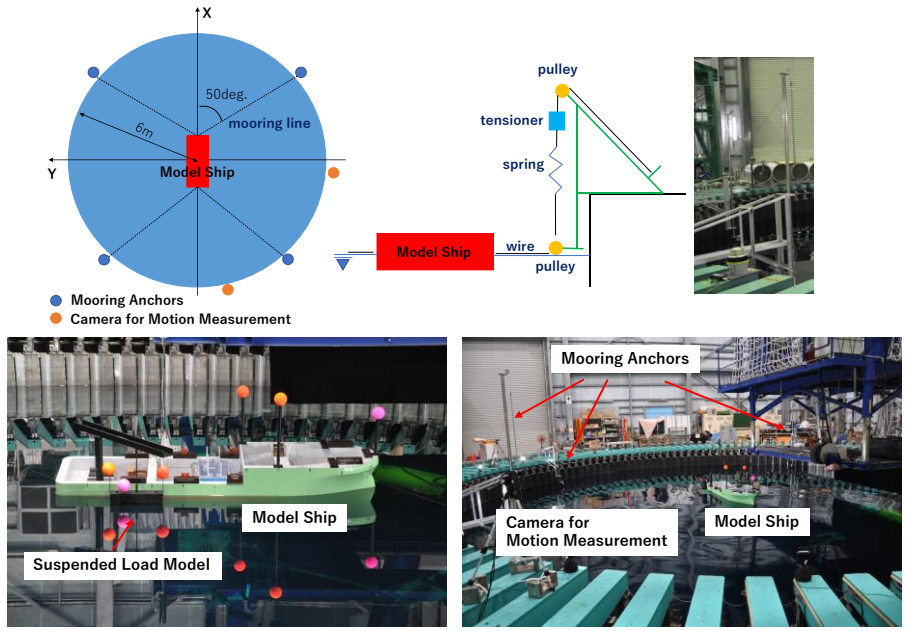

Figure 2: Configuration of mooring system and setup of model in Deepsea Basin.

Table 2: Wave Condition in model experiment (full scaled)

Wave	**Item**	**Value**
Regular Wave	Wave height [m]	0.6
	Wave period [s]	7.0, 7.5, 8.0, 9.0, 9.9
	Wave angle [deg.]	150, 120
Irregular Wave	Spectrum type	JONSWAP (gamma = 1)
	Significant Wave Height [m]	0.6
	Peak Period [s]	7.6
	Wave Angle [deg.]	150, 120

2.3 Experimental Results

In the case of regular wave, the amplitude of motion and wave height were analysed by Fourier transformation method and the response amplitude operator (RAO) of motions were calculated based on these amplitudes. On the other hand, in the case of irregular one, firstly the cross-spectrum between wave height and motion and autospectrum on wave height were calculated and the complex RAOs were derived based on the both cross- and auto-spectrums. The motion RAOs can be produced as the amplitude of the complex RAO.

Experimental results about motion RAOs for the OSV and the suspended load are shown in Figure 3. Mark and line mean the experimental results in regular and irregular wave respectively. Clearly the results of regular wave can be consistent with irregular one.

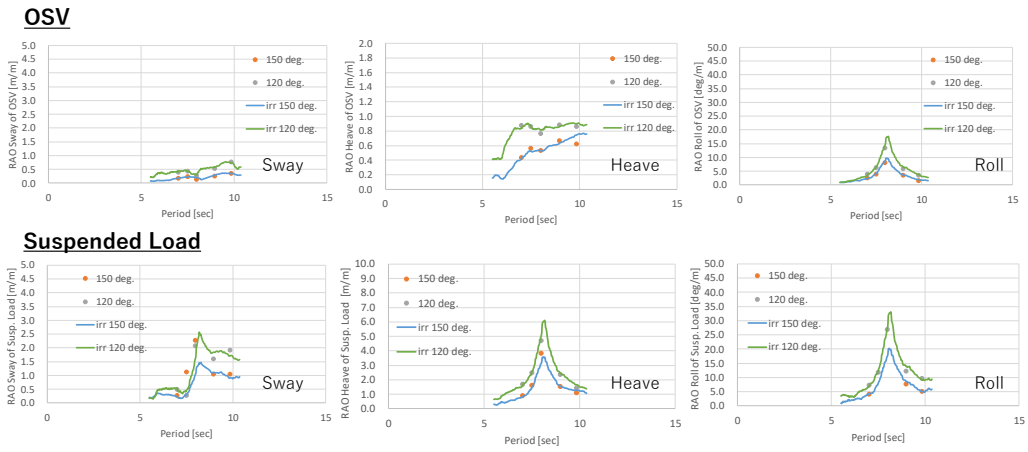

Figure 3: Motion RAOs for OSV and suspended load.

3 CFD SOLVER

Computing hydrodynamic force including viscous effect is important especially for non-streamlined body like subsea equipment installed by OSV since large vortex sheds at the angular edge of the equipment. Therefore, viscous CFD solver NAGISA developed in NMRI [8] was applied to compute hydrodynamic force acting on the OSV and suspended load. The motions of OSV and suspended load are coupled but moves independently with fulfilling the constrain conditions in very close position with each other. Therefore, it is difficult to apply grid morphing technique in this research because two body gird morphing in close position could dramatically increase the skewness of the grid cells which increase instability of the computation. To solve this problem, dynamic overset method [9] was applied by the overset grid assembling system UP_GRID also developed in NMRI [10]. Simplified introductions of the NAGISA and UP_GRID are described in this chapter. Check reference papers [8] and [10] for more detail about these software.

3.1 NAGISA

NAGISA is an unsteady Reynolds averaged Navier–Stokes solver with the structured overset grid method. A cell-centred finite volume method with structured grids is used for the spatial discretization. The velocity-pressure coupling is accomplished with the artificial compressibility approach. The inviscid fluxes are evaluated by MUSCL type 3rd-order upwinding scheme based on flux-difference-splitting, and the 2nd-order central differencing scheme is applied to the viscous fluxes. The symmetric Gauss-Seidel method is used to solve the system of equations. Following schemes are used for the time marching, the 2nd-order Euler backward differencing scheme for temporal time step and 1st-order Euler backward differencing scheme for pseudo time step. The full multigrid can be applied to get fast convergence. A single-phase localized level-set method is applicable for free surface treatment. Several turbulence models are selectable such as Spalart-Allmarase, k-ω SST, EASM including detached eddy simulation (DES). Wave model, body force propeller model, and manoeuvring model are also available for wide use of marine simulation. Uncouple motion model is already available in original software. NAGISA has amount of experience on resistance, propulsion and manoeuvring simulations validated with experimental results and showing better or equivalent accuracy comparing with popular commercial CFD software, i.e., [11] and [12].

3.2 UP_GRID

UP_GRID is a spline based overset grid assembling system based on the structured grid including several functions for overset assembling, i.e., grid generation, grid modification, and computing receptor-donor connectivity (RDC) which is necessary for the overset interpolation. Ferguson spline curve is applied to compute curves through grid points and cell centres for trimming grids and computing RDC. The basic algorithm of RDC computation starts from solving position inverse problem for each combination of the block which finds relative position in the spline space. Using the solution of position inverse problem, in-wall cells located inside the solid surface of the other blocks are identified and the cells surrounding the in-wall cells are defined as receptor cells which receive flow variables from the other blocks. The outer boundaries of each block are also set to be receptor cells to interconnect to the other blocks. After the receptor cells are settled, the non-in-wall and non-receptor cells vicinal to the other blocks' receptor cells are chosen to be donor cells which provide the flow variables to the receptor cells. The cells of higher prioritized block are preferentially defined to be donor. The dynamic overset method is implemented by modularizing the function of solving position inverse problem and RDC computation of UP_GRID and installed into NAGISA. UP_GRID also has many achievements using overset grid with NAGISA in several marine simulations validated with experimental results, i.e., [13].

3.3 Computational Grids

Overview of the computational grids for the overset grid method is summarised in Table 3 and Figure 4. Around 4 million cells in total of the all blocks in Table 3 but not all cells need to solve NS equations since higher prioritized blocks are responsible to solves NS equation in most of part of overlapped area. The dimensionless wall distance between body surface and first layer of the grid are kept to be y^+=100 since wall function [15] is applied on body surface in this simulation which could save the number of the grid. The grid

density on background grid is intentionally stretched to be very coarse near the back boundary to avoid reflection wave from the boundary. During the dynamic overset grid computation., All blocks except suspended load and background grids moves together following to the motion of the OSV keeping relative position between these grids so that could save overset computational time by skipping to solve the position inverse problem. Moreover, RDC computation between skeg, bilge keels and background are skipped for the purpose to avoid direct RDC relation between relatively fine resolution with high prioritized grid and coarse resolution with the lowest prioritized grid. Combination of these grids is prone to generate orphan cells.

Table 3: Summary of computational grids.

Grid	**i_m x j_m x k_m (grid points)**	**Priority**
Bilge Keel prt./stb.	19 x 129 x 17 (36,864) for each side	1, 2
Refinement for Bilge Keel prt./stb.	89 x 49 x 17 (67,584) for each side	3, 4
Skeg	31 x 121 x 17 (57,600)	5
Suspended Load	49 x 97 x 17 (73,728)	6
Refinement for Moon Pool	35 x 41 x 101 (136,000)	7
Hull	169 x 193 x 17 (516,096)	8
Refinement for Hull	121 x 73 x 121 (1,036,800)	9
Background	201 x 105 x 101 (2,080,000)	10

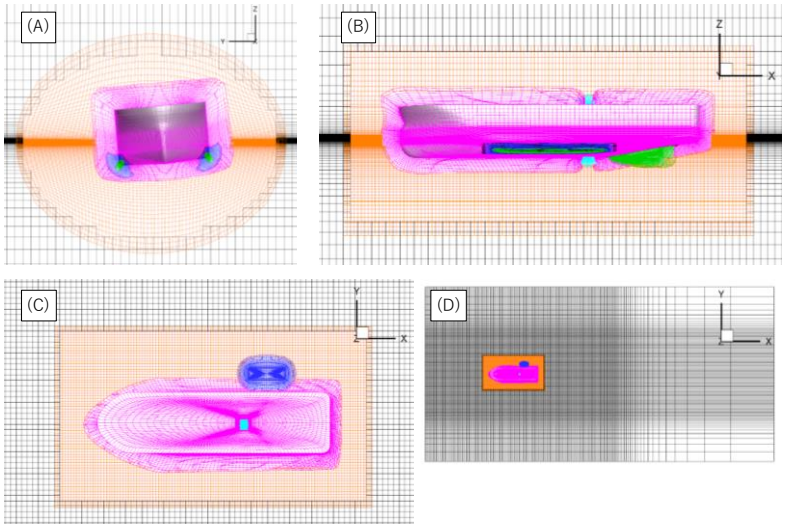

Figure 4: Mesh of body surface and slices of initial overset grid assemblies in head wave condition
(A): slice at midship; (B): slice at centre line; (C) slice at waterline;
(D) whole view of overset grid with slice at waterline.

3.4 CFD Conditions

Summary of the CFD conditions are shown in Table 4. In this research, Reynolds number is set to be 1.0×10^6 and characteristic velocity U is computed form kinematic viscosity of fresh water ν ($=1.0 \times 10^{-6}$ m^2/s) and length between perpendicular L_{PP}. Froude number is computed from U, L_{PP}, and gravity acceleration g ($=9.80665 m/s^2$) as 0.0805. Actual time step is set to be 1/50 of the wave period with 5 internal iteration. On body surface, viscous wall condition with wall function is applied, and y-symmetry condition is set on side boundaries to keep the quality of incident waves, Inflow condition with zero velocity is applied in front boundary of the OSV since no forward speed in model experiment. Outflow condition with zero velocity gradients is applied since waves are intentionally diffused by coarse region in the background grid. For turbulence mode, k-ω SST with wall function [15] is applied.

In wave conditions, initial wave height is set to be larger than that in experiment (=0.020m) since numerical diffusion could reduce wave height before wave reaches to the OSV. Initial heel angle is set to be -5.0 degrees which is almost equivalent to the experiment. Initial attitude of the suspended load is set to be

upright and same heading with the OSV. The heading angle 30.0 degrees match with wave angle 150 degrees in model experiment.

Table 4: CFD conditions.

Conditions		**Characteristic**	**Value (model scale)**
Basic		Reynolds number	1.0×10^6
		Froude number	0.0805
		Characteristic length [m]	2.5067 ($=L_{PP}$)
		Characteristic velocity [m/s]	0.3989
		Actual time step [s]	0.03
Boundary		Body surface	Viscous wall (wall function)
		Side	Y-symmetry
		Front	Inflow
		Back	Outflow
Wave		Height [m]	0.025
		Length [m]	3.330
		Period [s]	1.461
Initial Attitude	OSV	Heel [deg.]	-5.0
		Trim [deg.]	0.0
		Heading [deg.]	30.0
	Suspended Load	Heel [deg.]	0.0
		Trim [deg.]	0.0
		Heading [deg.]	30.0

4 MULTIBODY DYNAMICS SOLVER

The motions of OSV and suspended load have influence to each other motion and those motions cannot be modelled with simple pendulum model. To deal with these kinds of complex motion, multibody dynamics (MBD) could be one of the powerful solutions. Therefore, original MBD solver is developed and integrated into CFD solver NAGISA to obtain the coupled motions of OSV and suspended load.

4.1 Coordinate Systems & Constrain Conditions

Summary of coordinate systems and constrain conditions during the MBD simulation is shown in Figure 5. Note that dimension in Figure 5 is not drown correctly because for the visibility. Three types of coordinate systems are settled in the MBD solver. Frist coordinate system is global coordinate which origin (O in Figure 5) is fixed at the initial OSV position of cross point of midship, centre line, and water line with upright and straight-ahead condition. Second coordinate is OSV coordinate which origin (A in Figure 5) is fixed at the centre of gravity (CoG) of the OSV and move-rotate with her. The last coordinate is suspended load coordinate fixed at the CoG of the suspended load (B in Figure 5).

To reproduce the condition in the model experiment. The constrain conditions and the constrain connection point (CP) in MBD solver are set as in Figure 5. The mooring lines connected at the edge of her bow and stern (CP 3 and 6 in Figure 5) are reproduced as spring links. The opening angle between the 2 spring links is set to be 100 degrees as same as the model experiment. The height of the connection point of spring links on OSV (CP 3 and 6) is equivalent to the height of OSV CoG and the other connection potions of spring links are fixed on the global coordinate (CP 1, 2, 4, and 5). The connection between OSV and suspended load is rigid link which keeps specific distance between connection points of OSV and suspended load (CP 7 and 8 in Figure 5). All connection points of spring links (CP 1, 2, 3, 4, 5, and 6) are moment-free joint. The connection points of rigid link (CP 7 and 8) have yaw constrain as shown in section 4.3. The characteristics of the spring and rigid link are shown in Table 5. All links are massless since mass of these links in model experiments are

negligible compare to the mass of the OSV and the suspended load. The natural length of spring is set to be $3.0L_{PP}$ which is long enough to suspend the drift motion of the OSV. The initial stretch length of spring is determined to match with the initial tension of the mooring line in model experiment. Depending on the initial heading angle of the OSV, the positions of the spring link earth fixed points are properly rotated to keep the initial heading in calm condition. Here suspended position of the OSV (CP7 in Figure 5) is at (X_A, Y_A, Z_A) = (17.76m, 16.26m, 13.39m) in OSV coordinate in full scale.

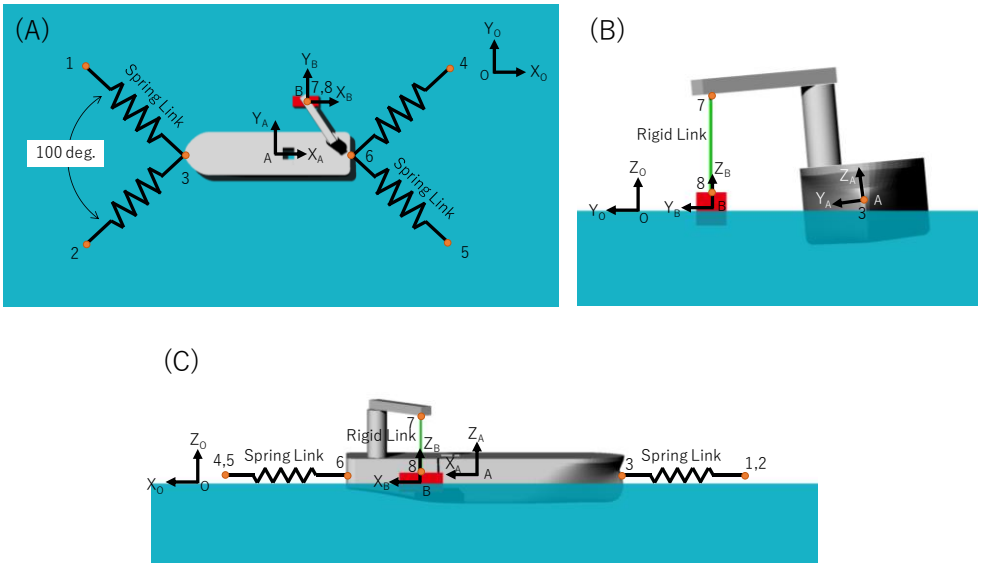

Figure 5: Definition of coordinate systems.
(A): top view (X_OY_O-plane); (B): front view (Y_OZ_O-plane); (C): side view (Z_OX_O-plane).

Table 5: Characteristics of spring and rigid link in MBD solver.

Link	**Characteristic**	**Value (model scale)**
Spring link	Mass [kg]	0
	Spring rate [N/m]	3.87
	Natural length [m]	7.52
	Initial stretch length [m]	0.63
Rigid link	Mass [kg]	0
	Length [m]	0.36

4.2 Equation of Coupling Motion

Equation of motion for constrained rigid multibody system can be developed from the principle of Jourdain [15] as Eq. (1) and (2)

$$\begin{bmatrix} \boldsymbol{M} & \boldsymbol{0} & \boldsymbol{\Phi}_V^T \\ \boldsymbol{0} & \boldsymbol{J}' & \boldsymbol{\Phi}_{\Omega'}^T \\ \boldsymbol{\Phi}_V & \boldsymbol{\Phi}_{\Omega'} & \boldsymbol{0} \end{bmatrix} \begin{bmatrix} \dot{\boldsymbol{V}} \\ \dot{\boldsymbol{\Omega}}' \\ \boldsymbol{\Lambda} \end{bmatrix} = \begin{bmatrix} \boldsymbol{F} \\ \boldsymbol{N}' - \widetilde{\boldsymbol{\Omega}}' \boldsymbol{J}' \boldsymbol{\Omega}' \\ -\dot{\boldsymbol{\Phi}}^{\boldsymbol{R}} \end{bmatrix} \tag{1}$$

$$\boldsymbol{\Phi} := \boldsymbol{\Phi}_V \boldsymbol{V} + \boldsymbol{\Phi}_{\Omega'} \boldsymbol{\Omega}' + \boldsymbol{\Phi}_{\overline{V\Omega'}} = \boldsymbol{0} \tag{2}$$

Here $\boldsymbol{M}$: mass matrix, $\boldsymbol{J}'$: inertia matrix, $\boldsymbol{V}$: velocity coordinate vector, $\boldsymbol{\Omega}'$: angular velocity coordinate vector, $\boldsymbol{\Lambda}$: Lagrange multiplier, $\widetilde{\boldsymbol{\Omega}}'$: cross product matrix operator of $\boldsymbol{\Omega}'$, $\boldsymbol{F}$: external force coordinate vector, $\boldsymbol{N}'$: external moment coordinate vector, $\boldsymbol{\Phi}$: velocity constrain matrix, $\boldsymbol{\Phi}_V$: $\boldsymbol{V}$ relative terms in $\boldsymbol{\Phi}$, $\boldsymbol{\Phi}_{\Omega'}$: $\boldsymbol{\Omega}'$ relative terms in $\boldsymbol{\Phi}$, $\boldsymbol{\Phi}_{\overline{V\Omega'}}$: remainder terms unrelated to $\boldsymbol{V}$ and $\boldsymbol{\Omega}'$ in $\boldsymbol{\Phi}$, and $\dot{\boldsymbol{\Phi}}^{\boldsymbol{R}}$is defined as Eq. (3) and (4).

$$\dot{\boldsymbol{\Phi}} = \boldsymbol{\Phi}_{\boldsymbol{V}}\dot{\boldsymbol{V}} + \boldsymbol{\Phi}_{\boldsymbol{\Omega}'}\dot{\boldsymbol{\Omega}}' + \frac{d\boldsymbol{\Phi}_{\boldsymbol{V}}}{dt}\boldsymbol{V} + \frac{d\boldsymbol{\Phi}_{\boldsymbol{\Omega}'}}{dt}\boldsymbol{\Omega}' + \frac{d\boldsymbol{\Phi}_{\overline{\boldsymbol{V\Omega}'}}}{dt} = \boldsymbol{0} \tag{3}$$

$$\dot{\boldsymbol{\Phi}}^{\boldsymbol{R}} := \frac{d\boldsymbol{\Phi}_{\boldsymbol{V}}}{dt}\boldsymbol{V} + \frac{d\boldsymbol{\Phi}_{\boldsymbol{\Omega}'}}{dt}\boldsymbol{\Omega}' + \frac{d\boldsymbol{\Phi}_{\overline{\boldsymbol{V\Omega}'}}}{dt} \tag{4}$$

To stabilize the computation and to keep accuracy of the constrain condition, Baumgarte stabilization method [16] is applied and Eq. (1) is transformed into Eq. (5).

$$\begin{bmatrix} \boldsymbol{M} & \boldsymbol{0} & \boldsymbol{\Phi}_{\boldsymbol{V}}^{\boldsymbol{T}} \\ \boldsymbol{0} & \boldsymbol{J}' & \boldsymbol{\Phi}_{\boldsymbol{\Omega}'}^{\boldsymbol{T}} \\ \boldsymbol{\Phi}_{\boldsymbol{V}} & \boldsymbol{\Phi}_{\boldsymbol{\Omega}'} & \boldsymbol{0} \end{bmatrix} \begin{bmatrix} \dot{\boldsymbol{V}} \\ \dot{\boldsymbol{\Omega}}' \\ \boldsymbol{\Lambda} \end{bmatrix} = \begin{bmatrix} \boldsymbol{F} \\ \boldsymbol{N}' - \widetilde{\boldsymbol{\Omega}}'\boldsymbol{J}'\boldsymbol{\Omega}' \\ -\dot{\boldsymbol{\Phi}}^{\boldsymbol{R}} - \alpha\boldsymbol{\Phi} - \beta\boldsymbol{\Psi} \end{bmatrix} \tag{5}$$

Here $\boldsymbol{\Psi}$:, position constrain, α, β: Baumgarte stabilization coefficients (=10 in this research). This simultaneous linear equation is solved with modified Cholesky (LDL^T) factorization. Moreover, fast and memory efficient sparse matrix solver PARDISO is also available using Intel Math Kernel Library [17] since the sparsity of the coefficient matrix in Eq. (5) increase in large system such as many bodies with many constrains.

4.3 Constrain Conditions

In this research massless spring link and massless rigid link are consider as the constrain for OSV and suspended load. The constrain force of spring link is included in external force and moment. For example, the constrain force and moment of spring link connecting CP 1 and 3 are shown as Eq. (6) and (7).

$$\boldsymbol{F}_{OA} = \boldsymbol{f}_{O3} = -\boldsymbol{f}_{O1} = \frac{\boldsymbol{C}_{OA}\boldsymbol{r}_{31}}{\sqrt{\boldsymbol{r}_{31}^T\boldsymbol{r}_{31}}}k\left(\sqrt{\boldsymbol{r}_{31}^T\boldsymbol{r}_{31}} - l\right) \tag{6}$$

$$\boldsymbol{N}'_{OA} = \tilde{\boldsymbol{r}}_{A3}\boldsymbol{C}_{OA}^T\boldsymbol{f}_{O3} \tag{7}$$

Here $\boldsymbol{f}_{Oi}$: constrain force coordinate vector at CP i, k: spring rate, l: spring natural length, $\boldsymbol{r}_{ij}$: position coordinate vector between CP i and j, $\tilde{\boldsymbol{r}}_{ij}$: cross product matrix operator of $\boldsymbol{r}_{ij}$, $\boldsymbol{C}_{IJ}$: coordinate transform matrix from I to J coordinate.

The rigid link connecting CP 7 and 8 can be expressed for position constrain $\boldsymbol{\Psi}$ in Eq. (8).

$$\boldsymbol{\Psi} = \frac{\boldsymbol{1}}{\boldsymbol{2}}\left(\boldsymbol{r}_{78}^T\boldsymbol{r}_{78} - {l_R}^2\right) = 0 \tag{8}$$

Yaw constrain between CP 7 and 8 can be represent in Eq. (9) for position constrain.

$$\boldsymbol{\Psi} = \frac{\boldsymbol{1}}{\boldsymbol{2}}\boldsymbol{\theta}_{78}^T\boldsymbol{\theta}_{78} = 0 \tag{9}$$

Here $\boldsymbol{\theta}_{ij}$ is relative yaw angle coordinate vector between CP i and j. Velocity and acceleration constrains of rigid link and yaw constrains ($\boldsymbol{\Phi}$ and $\dot{\boldsymbol{\Phi}}$) can be obtain by differentiating $\boldsymbol{\Psi}$ in Eq. (8) and (9).

4.4 Integration with CFD Solver

Taking hydrodynamic effects into multibody coupled motions, the developed MBD solver is modularized and integrated into CFD solver NAGISA. The computational process of NAGISA and MBD module is shown in Figure 6. In NAGISA, computed pressure on the body surface are integrated and transformed into force and moment in global coordinate and those hydrodynamic forces and moments are substitute into MBD module. In MBD module, the hydrodynamic forces and moments from NAGISA and

effects of gravity are added into external forces $\boldsymbol{F}$ and moments $\boldsymbol{N'}$ in Eq. (5) and coupling motions of bodies are computed by solving Eq. (5). The motions computed in MBD solver are return into NAGISA and the computational girds are moved according to the computed motions. When the relative positions of the blocks are changed, the overset information is updated by UP_GRID module and hydrodynamic forces are computed in new overset grids in next time step.

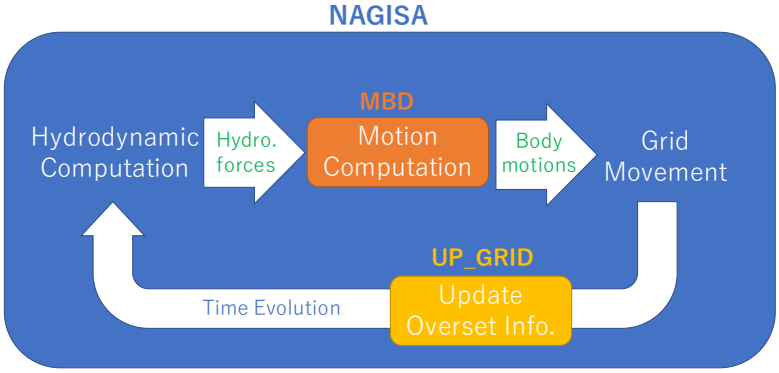

Figure 6: Relationship between NAGISA, MBD, and UP_GRID.

5 RESULTS AND DISCUSSIONS

The CFD simulations coupled with MBD are conducted with following procedure. First, OSV and suspended load are fixed in initial position without any motion. After incident wave fully developed and reach to the end of the boundary, motions of OSV and suspended load is gradually released during first 100 time step (around 2 wave encounter period) since sudden large motion could destabilize the computation. At the time of complete release (after 100 time step from motion starts), time: t is defined to be zero.

In this research, 2 cases are compared. One is coupling motion of OSV and suspended load as mention above, the other is fixing connection points of rigid link (CP 7 and 8 in Figure 5) so that OSV and suspended load move as one rigid body which means there is no relative motion between OSV and suspended load. Comparison of these 2 cases is appropriate to study the effect of the coupling motions. Hereinafter simulation case with OSV and suspended load coupling motion is called “FREE” case and simulation case without the coupling motion is called “FIX” case.

5.1 CFD and MBD Results

Figure 7 shows example of the flow field characteristics of FREE case (A) and FIX case (B) at t = 80 sec. in full scale, after 10 wave period from t = 0, after OSV motion conversed to periodic motion. Figure 7 shows free surface and pressure on body surfaces and iso-surface of the second invariants of the velocity gradient tensor: Q = 100 which usually demonstrates vortex region. Moreover, the surface of the iso-surface of Q=100 is contoured with vertical (Z_O direction in Figure 5) velocity. High pressure distribution can be seen around wave crest and vice versa which is reasonable pressure distribution in wave. Some vortex shedding from edge of bilge keels, suspended load, and moon pool can be found in both cases. Vortex shedding from moon pool are caused by the phase shift of water level elevation between the moon pool and incident wave elevation. Relatively narrow entrance of moon pool in OSV bottom cause shielding effect to delay the water level elevation from the incident wave. Aspelund et al. [18] observed similar vortex shedding from the moon pool edge using PIV in model experiment. As shown in Figure 7, large vortex shedding can be found around the suspended load which indicates that viscous effect needs to be taken into account to simulate accurate hydrodynamic forces acting on the non-streamlined body such as subsea equipment around splash zone.

Phase trajectories of OSV and suspended load heave and roll motions in FREE and FIX cases are presented in global coordinate in Figure 8. The phase trajectories for 6 wave period after ship motion converged into harmonic motion are shown in Figure 8. The heave trajectories of OSV and suspended load in global coordinate are shown in Figure 8(A). The heave motion of OSV in both FREE and FIX cases seem to be harmonic while the heave motion of FREE case shows slightly larger heave motion than that of FIX case. Moreover, in FREE case, heave motion of suspended load is larger than that of OSV and the motion does not appear to converge to the harmonic oscillation but seems to be chaotic. In Figure 8(B), The roll motion of OSV

and suspended load in FREE and FIX cases are presented. While the roll motion of OSV in FIX case appear to harmonic, the roll motion of OSV in FREE case seem to be subharmonic and larger than that of FIX case. Large double perioded roll motion (3 cycles during 6 wave periods) can be seen in roll motion of suspended load in FREE case which could affect the OSV roll motion. According to these motion analyses, even in regular wave, coupling motion of the suspended load seems to be chaotic or subharmonic as similar with double pendulum motion which is well known that can be easily developed into chaotic motion. Ellermann et al. [19] applied bifurcation analysis of subharmonic and chaotic motion of suspended load and crane vessel.

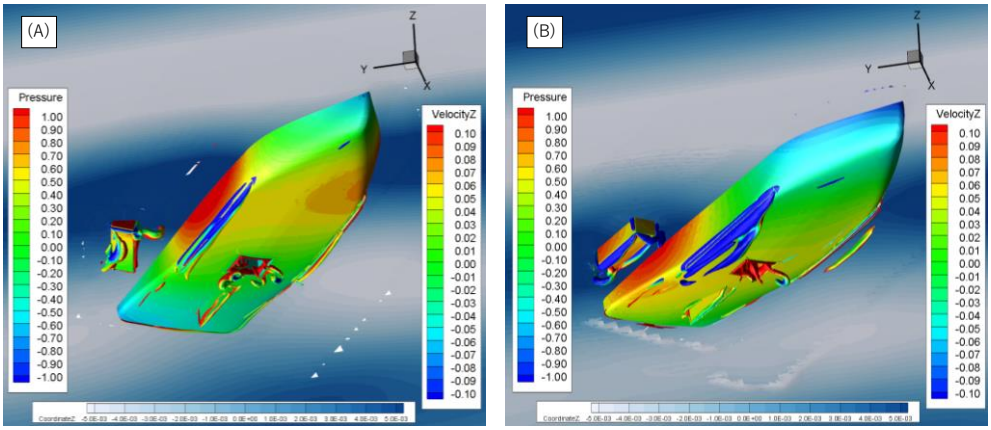

Figure 7: Free surface, pressure on the body surface, and Q=100 iso-surface in head quartering wave; (A): FREE case; (B): FIX case.

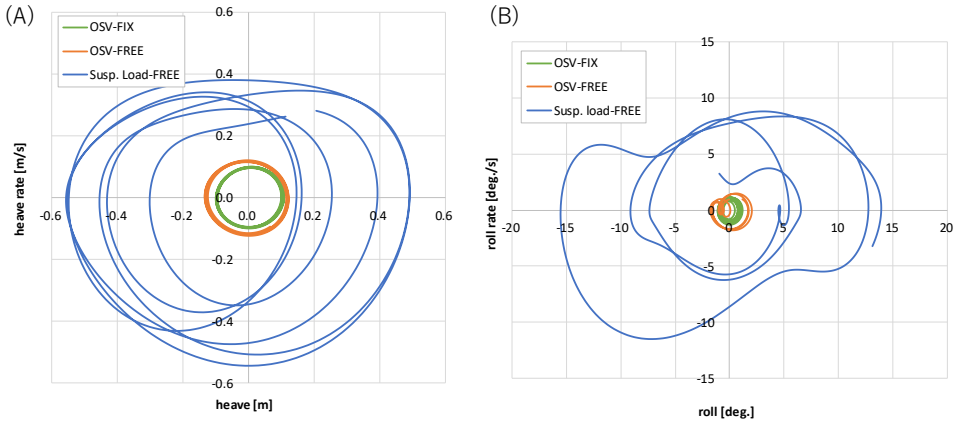

Figure 8: Phase trajectories of OSV and suspended load motion in FREE and FIX case; (A): heave motion; (B) roll motion.

5.2 Comparison Between CFD and Experiment Results

Comparison of OSV and suspended load motions between experiment and CFD in FREE and FIX cases in global coordinate are shown in Figure 9. Note phase between CFD and experimental results are shifted for easier visibility. In Figure 9(A), CFD shows relatively smaller OSV heave motion than experiment in both FREE and FIX cases. These could be because of numerical diffusion of incident wave which could reduce the wave height of the wave. Since wave height of the experiment is 0.6m in full scale while wave height in CFD shows around 0.55m near OSV. This gap between experiment and CFD can be reduced by using finer background mesh to prevent large numerical diffusion of incident wave. In Figure 9(B), heave motion of suspended load in FREE case also shows smaller amplitude than that of experiment since the heave motion of suspended load is induced by ship motion. Moreover, CFD suspended load motion seems to include some subharmonic or double period motion while experimental motion shows harmonic motion. In Figure 9(C), CFD FREE cases shows smaller harmonic roll motion than experiment and large subharmonic motion as already mentioned in Figure 8(B) while experiment shows merely harmonic motion. In Figure 9(D), roll motion of CFD suspended load shows larger roll motion than that of experiment with double wave period while experimental roll motion shows harmonic motion. This large subharmonic roll motion could affect roll motion of OSV and heave motion of suspended load which including both harmonic and subharmonic motion.

The large difference of roll motion of suspended load between experiment and CFD could be because of nonnegligible structural damping of connection point of rigid link in experiment. Since, in CFD/MBD simulation, it is assumed that pitch and roll moment of CP 7 and 8 in Figure 5 are free while there should be some structural damping in actual mechanical joint in the experiment. Therefore, further primitive validation with free damping test should be done to estimate structural damping at connection points and new constrain model need to be developed to include structural damping at connection point. After that more validation is required with other wave periods and heading angles in future works to develop reliable simulation model.

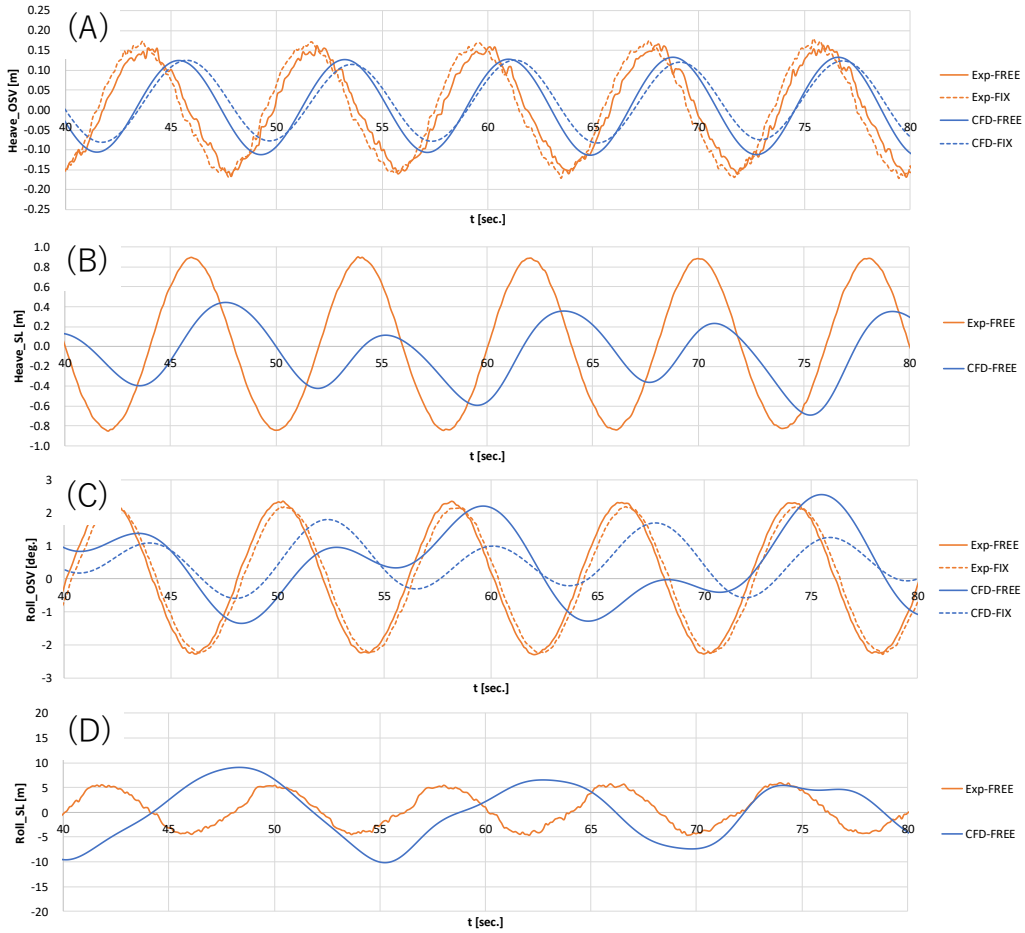

Figure 9: Comparison of heave and roll motion of OSV and suspended load between experiments and CFD; (A): OSV heave motions; (B): suspended load heave motion; (C): OSV roll motions; (D): suspended load roll motion

6 CONCLUSION AND FUTURE WORK

Model experiment and CFD simulation of OSV with suspended load in wave were conducted. To simulate coupled motion of OSV and suspended load, the multibody dynamics solver was developed from the principle of Jourdain and several constrain conditions were set to mimic the experimental conditions such as spring and rigid links. The multibody dynamic solver was modularized into CFD solver NAGISA developed by NMRI to compute multibody dynamics and unsteady CFD in same time. Dynamic overset gird method was applied to reproduce the coupling motions of OSV and suspended load whirling near the OSV.

During the CFD simulation, the suspended load shows chaotic motion in OSV coordinate and large vortex shedding from the edge of the suspended load. It indicates dynamic coupling of multibody dynamics and viscous CFD is necessary for lifting/lowering simulation. The CFD results are validated with the experimental results while motion in CFD shows smaller OSV motion and larger suspended load motion than those of experiment because of numerical diffusion of incident wave and omitting structural damping at connection points. Therefore, further investigations and validation need to be done with finer background mesh

and constrain model including structural damping. Moreover, validation in other wave period and heading angle is also required in future works.

ACKNOWLEDGEMENTS

Authors deeply appreciate Hiroshi Kobayashi of CFD research group, Fluid Engineering & Ship Performance Evaluation Department, NMRI for beneficial discussion and advice on dynamic overset grid method and UP_GRID.

REFERENCES

[1] Schellin T. E. et al., 1989, Crane ship response to regular waves: linearized frequency domain analysis and nonlinear time domain simulation, Proceedings of the eighth international conference on offshore mechanics and arctic engineering.

[2] Hannan M.A. and Bai W., 2015, Nonlinear hydrodynamic responses of submerged moving payload in vicinity of a crane barge in waves, Marine Structures, Vol. 41, pp.154-179.

[3] Hong J. W. et al., 2015, Offshore Installation of Subsea Equipment Considering Elasticity of the Crane Boom in Harsh Environment, Proceedings of the 25th International Ocean and Polar Engineering Conference, pp. 1284-1289.

[4] Jeong D. H. et al., 2016, Lifting simulation of an offshore supply vessel considering various operating conditions, Advances in Mechanical Engineering, Vol. 8(6), pp. 1-13.

[5] Cha J. H. et al., 2010, Dynamic response simulation of a heavy cargo suspended by a floating crane based on multibody system dynamics, Ocean Engineering, Vol. 13, Issue 14-15, pp. 1273-1291.

[6] Solaas, F et al., 2017, Dynamic Forces and Limiting Sea States for Installation of GRP Proetion Covers, Proc. of the 36th International Conference on OMAE, June 25-30, Trondheim, Norway, OMAE2017-62499.

[7] The Construction Vessel Register 2011, Clarkson.

[8] Ohashi K. et al., 2018, Development of a structured overset Navier–Stokes solver with a moving grid and full multigrid method, Journal of Marine Science and Technology.

[9] Carrica P. M. et al., 2007, Ship motions using single-phase level set with dynamic overset grids, Computer & Fluids, vol. 36, pp.1415–1433

[10] Kobayashi H., Kodama Y., 2016, Developing Spline Based Overset Grid Assembling Approach and Application to Unsteady Flow Around a Moving Body, Journal of Mathematic and System Science, Vol. 6, pp. 339-347.

[11] Larsson L.et al., Proceedings, 2015, Tokyo 2015 Workshop on CFD in Ship Hydrodynamics.

[12] Stern F. et al., 2011, Experience from SIMMAN 2008—The First Workshop on Verification and Validation of Ship Maneuvering Simulation Methods, Journal of Ship Research, Vol. 55, Number 2, pp. 135-147 (13).

[13] Araki M. et al., 2015 Effects of Rudder Horn and Propeller Hub Vortex for CFD Manoeuvring Simulations; Proceedings of MARSIM2015; Session4-1.

[14] Ohashi K., Hino T., 2012, Numerical study on the applicability of wall function models for the flows around an appendage attached to a body, AIAA 50th Aerospace Science Meeting Papers, AIAA 2012-0445.

[15] John Papastavridis. On Jourdain's principle. International Journal of Engineering Science, Elsevier,1992, 30, pp.135 - 140.

[16] Baumgarte J., 1972, Stabilization of Constraints and Integrals of Motion in Dynamical Systems, Computer Methods in Applied Mechanics and Engineering, Vol. 1, pp. 1–16.

[17] Intel Corporation, 2019, Intel Math Kernel Library, https://software.intel.com/sites/default/files/mkl-2019-developer-reference-fortran_0.pdf

[18] Aspelund L., Pettersen B., Visscher J., and Naess I. T. B., 2014, Hydrodynamic forces acting on objects in a moonpool, Proceedings of the 33rd International Conference on Ocean, Offshore and Arctic Engineering, OMAE2014-24694.

[19] Ellermann K., Kreuzer J. E., and Markiewicz M., 2002, Nonlinear dynamics of floating cranes, Nonlinear Dynamics, Vol. 27, Issue 2, pp. 107-183.